RESEARCH ARTICLE

ADVANCED ELECTRONIC MATERIALS
www.advelectronicmat.de

Chemical Dopant-Free Doping by Annealing and Electron Beam Irradiation on 2D Materials

Min Sup Choi, Myeongjin Lee, Tien Dat Ngo, James Hone, and Won Jong Yoo**

Doping is a key technique for forming complementary metal-oxide-semiconductor (CMOS) that is a basic building block for current state-of-the-art semiconductor devices. However, conventional doping methods such as ion implantation are unsuitable for 2D materials due to their ultra-thinness to accommodate substitutionally doped atomic structures and vulnerability to high energy ion bombardment. Chemical doping methods have been widely used for 2D materials to induce a charge exchange transfer; however, they are subjected to surface contamination which can be detrimental for high quality semiconductor device processing. In this work, the authors reveal the effects of chemicals-free doping in which annealing induces a p-doping effect by physisorption and substitution of oxygen atoms while electron beam irradiation selectively n-dopes $MoTe_2$, based on the results obtained by electrical characterization and Kelvin probe force microscopy. The annealing increases work-function of $MoTe_2$ which undergoes oxidation as observed in the reduction of surface potential and the transition of transfer curves toward the p-type behavior. Electrical measurements and a significant reduction in surface potential after electron beam irradiation indicate the generation of trapped charges which is responsible for the n-doping effect. Subsequently, the authors fabricate a CMOS inverter consisting of distinctively p- and n-doped areas of $MoTe_2$.

1. Introduction

2D semiconductors are promising materials for next generation electronics due to their large carrier mobility and sizable bandgaps.[1] Ultra-thinness of 2D materials presents a great potential for wearable electronic devices and biomedical applications such as human motion and physiological detection that cannot be easily realized with conventional Si technologies.[2] To realize advanced semiconductor electronics, high-quality doping methods must be developed to minimize contact resistance while controlling carrier types and threshold voltages in field effect transistors (FETs). Conventional ion implantation is known to generate unwanted structural defects in 2D materials.[3] In addition, recently developed chemical doping methods to apply to 2D devices can contaminate the surface of materials.[4] They are also unsuitable for spatial doping control on the areas with nanoscale dimension. Thus, selective doping techniques that are clean with minimal-damage are required imperatively for 2D materials to be implemented in complementary metal-oxide-semiconductor (CMOS)-compatible technologies.

2H-molybdenum ditelluride ($MoTe_2$) is one of the 2D semiconducting transition metal dichalcogenides (TMDCs) with a comparable bandgap (0.8 eV for bulk and 1.1 eV for monolayer)[5,6] to Si. It is a potential candidate for post-Si electronics as well as low-power consumption devices such as tunneling devices due to its smaller bandgap than most of other TMDCs. Several doping approaches have been proposed for $MoTe_2$ to modulate its electrical properties and realize CMOS inverters, including annealing,[7,8] atomic layer deposition of Al_2O_3,[9,10] oxygen plasma treatments,[11] and laser/electron-beam (e-beam) irradiation.[12–14] Among these methods, the effect of e-beam irradiation on electrical properties needs to be investigated carefully since e-beam lithography is a very widely used patterning technique to fabricate 2D devices. Several different mechanisms for modulating electrical properties of 2D materials by e-beam irradiation have been proposed, including phase transition from 2H to 1T phase,[15,16] defect creation,[17,18] and generation of interface trap charges.[19,20] It is generally known that e-beam with a high energy (>60 keV) used for transmission electron microscopy imaging can induce phase transition and defects while that with a low energy tends to generate interface charges. However, the mechanism responsible for doping effects has not been clearly understood yet.

In this work, we developed a clean chemical-free doping method for $MoTe_2$ by annealing and e-beam irradiation. It was found that annealing induced p-doping while e-beam irradiation induced n-doping in $MoTe_2$ FETs. Annealed p-$MoTe_2$

Dr. M. S. Choi, M. Lee, T. D. Ngo, Prof. W. J. Yoo
SKKU Advanced Institute of Nano Technology
Sungkyunkwan University
Suwon, Gyeonggi-do 16419, Korea
E-mail: goodcms@skku.edu; yoowj@skku.edu

Dr. M. S. Choi, Prof. J. Hone
Department of Mechanical Engineering
Columbia University
New York, NY 10027, USA

The ORCID identification number(s) for the author(s) of this article can be found under https://doi.org/10.1002/aelm.202100449.

DOI: 10.1002/aelm.202100449

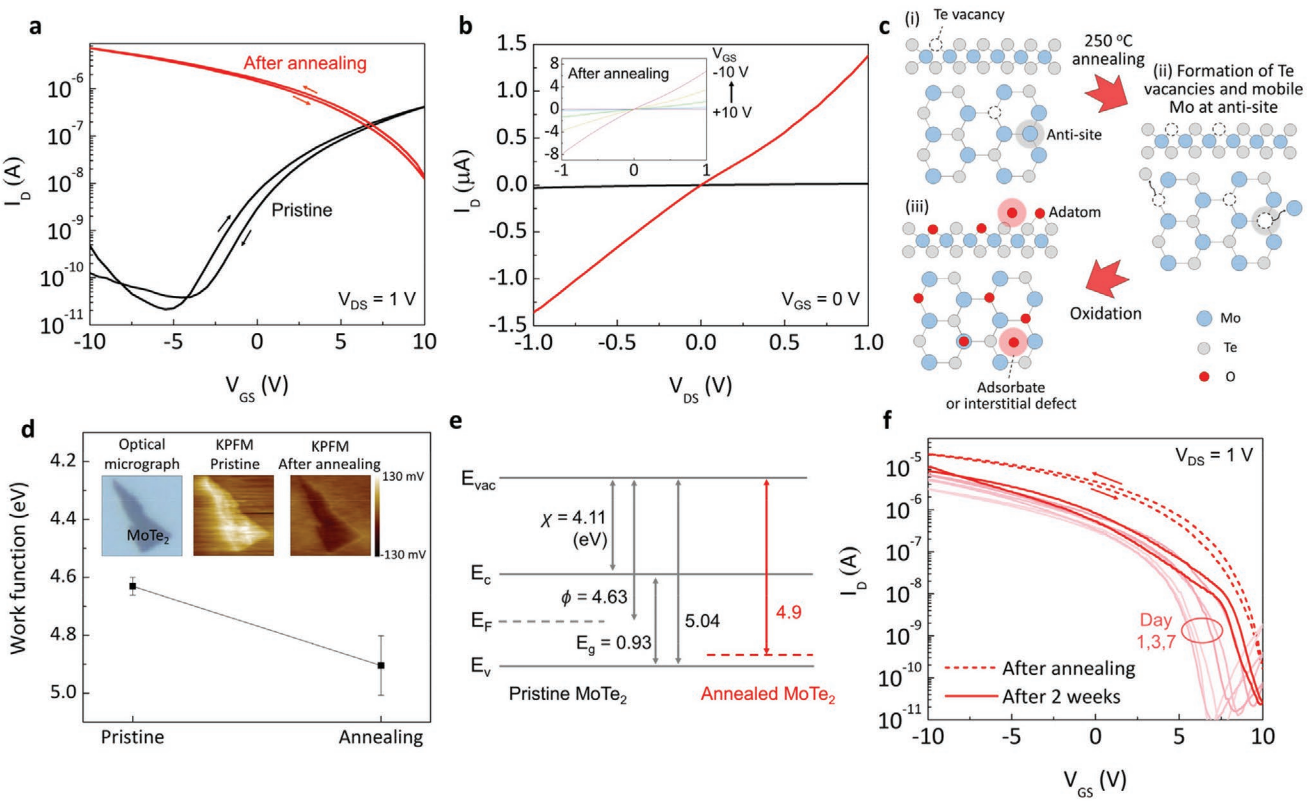

Figure 1. Annealing effects on $MoTe_2$. a) Transfer and b) output curves of $MoTe_2$ transistor before and after annealing. The inset in (b) shows output curves at different V_{GS} after annealing. c) Schematic illustration of annealing and oxidation effects on $MoTe_2$ atomic structure. d) Work-function for pristine and annealed $MoTe_2$ measured by KPFM. Error bar indicates the standard deviation calculated from five measured samples. e) Band-structure of pristine and annealed $MoTe_2$. It was constructed according to KPFM results. f) Transfer curves of the device measured after annealing (dotted) and at 2 weeks after annealing (solid).

further underwent a transition to n-type semiconductor with multiple loops of e-beam exposure. Kelvin probe force microscopy (KPFM), Raman spectroscopy, and electrical characterizations unveiled the underlying mechanism of each doping effect. Most of all, this work found that the doping mechanism responsible for trapped charges at interfaces induced by e-beam irradiation could be universally extended to other 2D materials such as graphene and WSe_2 without chemical processing-induced contamination. Finally, we fabricated $MoTe_2$ CMOS inverters composed of p- and n-FETs realized by annealing with subsequent e-beam irradiation.

2. Results and Discussion

We first investigated the effect of annealing on transfer curves of $MoTe_2$ device, as shown in **Figure 1**a. Rapid thermal annealing (RTA) system was used at 250 °C under 5 mTorr pressure for this work. Before annealing, the device showed an n-type semiconducting behavior while its conversion to p-type was observed after 3-h annealing. Hysteresis was considerably reduced while ON current was enhanced by a few orders of magnitude due to surface cleaning and doping effects. Output characteristics of the same device clearly showed a linear behavior with increased I_D after annealing as shown in Figure 1b. Our group has previously reported that $MoTe_2$ is very sensitive to oxygen (O_2) molecules at elevated temperatures due to: i) its intrinsic defects such as Te vacancies and anti-site defects as illustrated in Figure 1c, resulting in physical and chemical absorption.[7] In this report, besides the Mo 3p peaks of bulk pristine $MoTe_2$, two additional peaks appeared in the X-ray photoelectron spectroscopy (XPS) spectra after 250 °C annealing at 4 mTorr using the same RTA system used in this study, representing the oxidation states of MoO_3 or MoO_x suboxides. Thus, we believe that the similar oxidation occurred in our annealing process given the similar annealing temperature and pressure (250 °C and 5 mTorr); Coelho et al. also reported that ii) more Te can be vacancies formed and excessive Mo atoms on Te site (anti-site) can be mobile at elevated temperature (500 K), resulting in empty Te sites;[21] thus, iii) the O_2 molecule that can act as electron acceptor due to its large electronegativity tends to fill the empty Te sites and adsorbed onto the top layer as adsorbates and adatoms. Likewise, we observed a p-type transition of $MoTe_2$ by annealing, suggesting that absorbed oxygen atoms withdrew electrons from $MoTe_2$.

To further investigate the p-doping effect by annealing, we conducted KPFM measurements before and after annealing, as shown in Figure 1d. Insets show optical micrograph and surface potential map obtained by KPFM of representative $MoTe_2$ before and after annealing. We observed a clear reduction in surface potential after annealing, indicating an increased work-function according to the following equation, $-eV_{CPD} = \varphi_{tip} - \varphi_{sample}$, where V_{CPD} is the contact potential difference between the tip and the sample, and φ_{tip} and φ_{sample} are work-functions of the tip and the sample, respectively.[22] An external bias (V_{ext}) was applied to the tip to nullify V_{CPD}, $\varphi_{sample} = \varphi_{tip} - eV_{ext}$, where V_{ext} is equivalent to the measured potential in the KPFM potential map. Thus, the reduction in potential represented an increased work-function of sample. With the known work-function of HOPG (about 4.65 eV) as a reference, the averaged work-function of multiple $MoTe_2$ samples changed from 4.63 to 4.9 eV after annealing, confirming the p-doping effect.

According to the change in work-function, we extracted Fermi energy of $MoTe_2$ as shown in Figure 1e. Values of electron affinity (χ), bandgap (E_g), and valence band edge position (E_v) were obtained from local density approximation.[23] Before annealing, the Fermi energy was located at the middle of the bandgap despite its n-type behavior observed from electrical measurements due to a Fermi-level pinning effect.[24] A significant Fermi energy shifting toward the valence band edge due to a p-doping effect was expected after annealing. The hole carrier density could be estimated with the above information from the following equation: $p = g_{2D}k_B T \ln\{1+\exp[(-(E_F - E_v)/k_B T]\}$, where g_{2D} is the density of state, k_B is the Boltzmann constant, and T is the temperature.[25] The calculated density was 4.44×10^{10} cm^{-2}, which was in reasonable agreement with the density from the Drude model (8.21×10^{10} cm^{-2} in Table S1, Supporting Information). A slight discrepancy might be attributed to the contact resistance since we conducted only two-probe measurements. Further four-probe measurements will be helpful to improve the accuracy of carrier density.

A slight degradation of p-type behavior was observed when the device was remeasured on the next day as shown in Figure 1f. This might be due to dissociation of physically adsorbed oxygen atoms, for example, adsorbates in Figure 1c. Nevertheless, the annealed $MoTe_2$ still preserved its p-type semiconducting characteristic even after 2 weeks of air exposure and barely changed during the measurement period with robustness of chemically bonded oxygen atoms. The same p-doping effect observed from multiple devices after annealing further demonstrates its stability and reproducibility as shown in Figure S1, Supporting Information.

Next, we investigated the effect of e-beam irradiation on $MoTe_2$ device. **Figure 2**a shows optical microscopic image and cross-sectional schematic diagram of $MoTe_2$ FETs after e-beam exposure. The $MoTe_2$ used for this work had a thickness less than 5 nm (mostly 3-layer (3L)), which was confirmed by atomic force microscopy (AFM) and optical contrast. Figure 2b shows room temperature transfer characteristics of the e-beam irradiated device measured at $V_{DS} = 1$ V. Various beam area doses (400

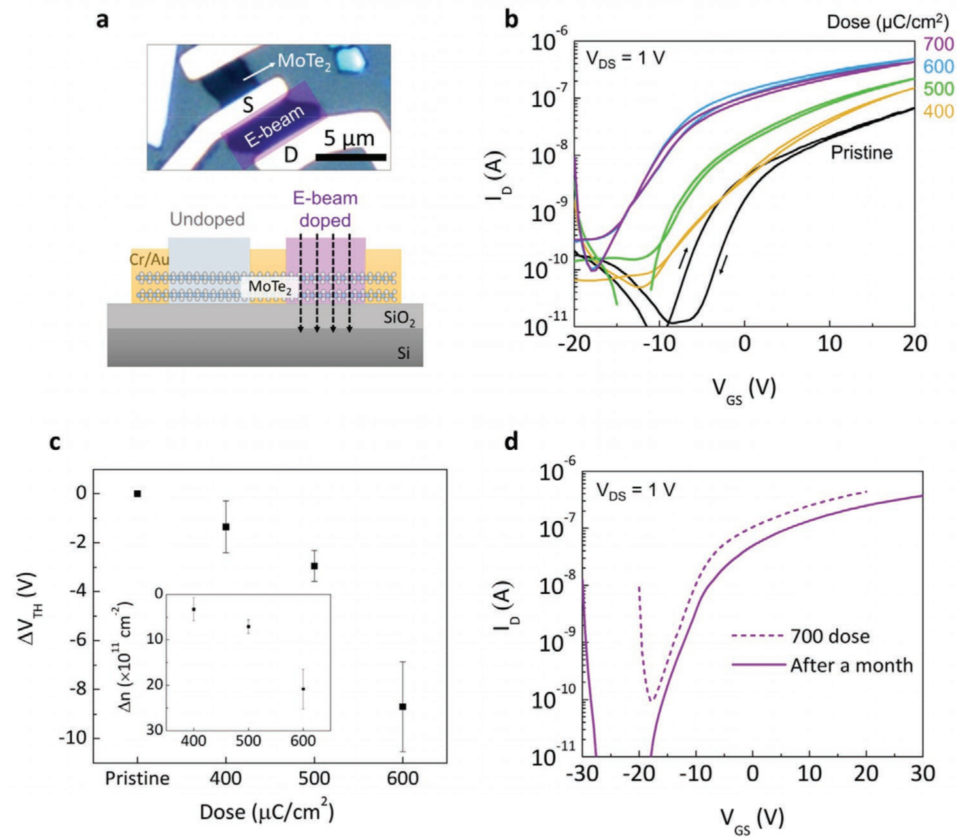

Figure 2. Effect of e-beam irradiation on $MoTe_2$ transistor. a) Optical microscopic image and schematic cross-section of $MoTe_2$ transistor. b) Transfer characteristics of the pristine state and e-beam irradiated devices at $V_{DS} = 1$ V. E-beam irradiation dose varied from 400 to 700 µC cm^{-2}. c) Threshold voltage shift and corresponding doping density for e-beam irradiated $MoTe_2$ with beam area dose of 400, 500, or 600 µC cm^{-2}. d) Transfer characteristic of e-beam irradiated $MoTe_2$ transistor with beam area dose of 700 µC cm^{-2} after 1 month, showing the robustness of doping.

Table 1. Summary of various doping techniques of 2D materials for a benchmark. The carrier densities were estimated from the KPFM, V_{TH} shift, and Drude model ($n = \sigma/q\mu_{FE}$).

Doping techniques	Materials	Thickness	Processing conditions	Type	V_{TH} shift [V]	Carrier (doping) density [10^{11} cm^{-2}]	References
Annealing	$MoTe_2$	3L	250 °C, 3 h	N → P	–	0.82 (Drude), 0.44 (KPFM)	This work
	$MoSe_2$	≈2.6–3.7 nm	UV-ozone + 60 °C, 3 cc min^{-1}, 2 mins	N → P	–	0.1 to 1 (Drude)	[32]
	$PdSe_2$			Ambi → P	25	10 (Drude)	
	$MoTe_2$			Ambi → P	-	100 (Drude)	
E-beam irradiation	$MoTe_2$	3L	20 kV, 600 μC cm^{-2}	N	–8.7	20.8 (V_{TH} shift)	This work
	Graphene	1L	2 kV, 16 μC cm^{-2}	N	–53	40 (V_{TH} shift)	[33]
			30 kV, 160 μC cm^{-2}	P	11	8.3 (V_{TH} shift)	
	CVD MoS_2	1L	30 kV, 800 μC cm^{-2}	N	–10	7.2 (V_{TH} shift)	[34]
	$MoTe_2$	10L (7.2 nm)	2 kV, 8082 μC cm^{-2}	N	–20	16 (V_{TH} shift)	[14]
Proton beam irradiation	MoS_2	12L (8.5 nm)	10 MeV, 16 μC cm^{-2}	P	3	7.2 (V_{TH} shift)	[35]
UV light illumination +V_{GS}	$MoTe_2$/*h*-BN	28 nm	λ = 254 nm, 2.5 mW cm^{-2}, 1 s, V_{GS} = –60 V	N	–45	45 (Drude)	[36]
			λ = 254 nm, 2.5 mW cm^{-2}, 1 s, V_{GS} = +60 V	N → P	–	50 (Drude)	
Laser irradiation	$MoTe_2$	17.4 nm	λ = 532 nm, 4 mW, integration time = 0.5 s	P	37	26.6 (V_{TH} shift)	[13]
ALD Al_2O_3	CVD $MoTe_2$	3L	3 nm Al_2O_3 deposition	N	–80	57.5 (V_{TH} shift)	[10]
O_2 plasma	$MoTe_2$	5.4 nm	ICP, 20 Pa, 30 sccm flow, 20 W, 400 s	P	–	100 (Drude)	[11]

to 700 μC cm^{-2}) at an acceleration voltage of 20 kV were used. We found that e-beam exposure gradually enhanced the drain current (I_D) from 0.7×10^{-7} to 5×10^{-7} A at positive V_{GS} and shifted threshold voltage (V_{TH}) towards negative V_{GS} as dose increased and saturated at 600 μC cm^{-2}, indicating an n-doping effect. Furthermore, the OFF-current was also increased as the e-beam dose increased due to enhanced tunneling at OFF-state attributed to band bending near the contact by the doping effect.[26] It is noted that gate leakage current remained unchanged at the noise floor despite an e-beam irradiation, indicating that gate leakage current was not responsible for the increased I_D and OFF-current (see Figure S2, Supporting Information). We extracted V_{TH} shift and corresponding doping density as shown in Figure 2c. Mean ΔV_{TH} decreased from –1.35 to –8.7 V as dose increased from 400 to 600 μC cm^{-2}. Corresponding doping densities ($\Delta n = C_{ox} \times \Delta V_{TH}/q$, where C_{ox} is the oxide gate capacitance and q is the elementary charge)[27] ranged from 0.32×10^{12} to 2.08×10^{12} cm^{-2}. Taking the number of electrons estimated from beam area doses (2.5×10^{15} #/cm^2, 3.13×10^{15} #/cm^2, and 3.75×10^{15} #/cm^2 for 400, 500, and 600 μC cm^{-2}, respectively) into account doping efficiencies were estimated to be 0.013%, 0.023%, and 0.056%, respectively.

As aforementioned, several mechanisms have been suggested to explain doping effects. Phase transition in 2D materials can be easily characterized by Raman spectroscopy which revealed different vibration modes compared to the pristine state due to structural distortion. We conducted Raman spectroscopy on 1L- and 3L-$MoTe_2$. Results are shown in Figure S3, Supporting Information. Typical Raman modes of 2H $MoTe_2$ such as A_{1g} and E^1_{2g} were observed while no clear evidence of 1T′ phase at ≈120 cm^{-1} was observed for e-beam irradiated samples,[28,29] suggesting that the doping mechanism did not rely on phase transition. Defects such as Te vacancies in $MoTe_2$ are known to induce n-doping effects, supporting a defect-assisted doping.[30] However, defects tend to attract O_2 or H_2O molecules resulting in p-doping upon air exposure.[8,31] Our e-beam doped $MoTe_2$ did not show any strong degradation or p-type behavior after 1 month of air exposure as shown in Figure 2d, further excluding defect-assisted doping. The slightly increased thickness by ≈0.5 nm in AFM topography (Figure S4, Supporting Information), presumably due to weak oxidation by e-beam irradiation, also suggests a minimal damaging process, unlike the high energy laser exposure that usually results in a reduced layer thickness.[12] The doping mechanism of e-beam irradiation is further discussed in KPFM measurements.

Table 1 summarizes the electrical parameters such as carrier type, V_{TH} shift and carrier density, obtained from various 2D materials and doping techniques. Our work provided a comparable doping density estimated from the Drude model and KPFM measurements to the annealed $MoSe_2$, however, relatively lower than other p-doping techniques, requiring a further study to enhance the density. Nevertheless, our e-beam irradiation gave a clear n-doping effect in terms of doping density comparing to other n-doping methods such as beam (or light) irradiations. The higher n-doping density induced by e-beam irradiation than p-doping induced by annealing enabled the fabrication of CMOS inverter as discussed later.

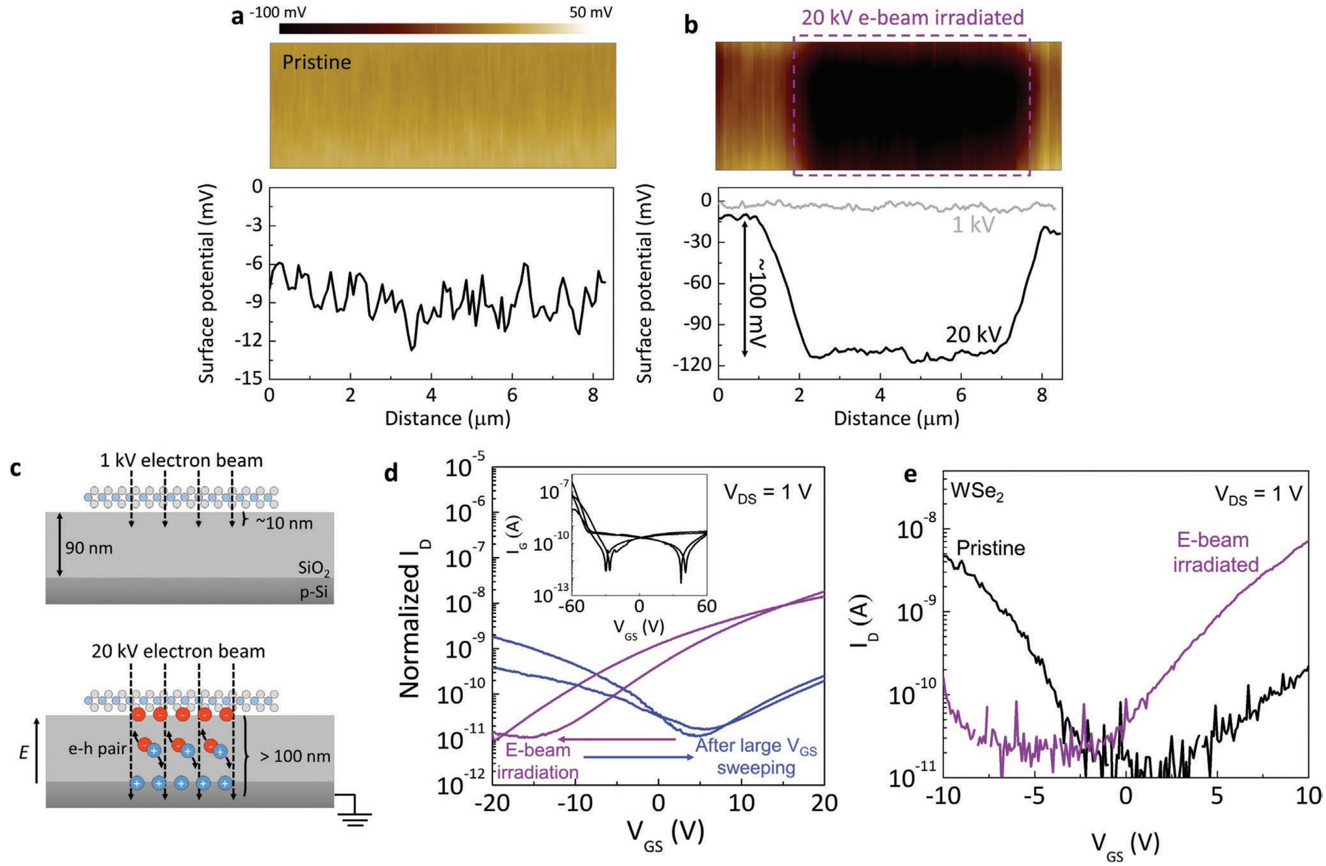

Figure 3. Doping mechanism of e-beam irradiation. Surface potential mapping measured by KPFM for a) pristine and b) e-beam irradiated 1L-$MoTe_2$ with two different acceleration voltages, 1 (gray) and 20 kV (black). c) Schematic diagrams to illustrate penetration depth with different e-beam energy and formation of fixed charges at interfaces induced by electron–hole pairs. d) Transfer curves of $MoTe_2$ transistor with repeated e-beam irradiation and large V_{GS} sweeping to demonstrate the influence of charge trapping and de-trapping. The inset shows I_G versus V_{GS} for the increased range of V_{GS} sweeping. e) Transfer curves obtained at $V_{DS} = 1$ V for the pristine and e-beam irradiated WSe_2 devices.

To explore the underlying doping mechanism of e-beam irradiation, we further measured surface potential of selectively e-beam irradiated $MoTe_2$. **Figure 3** shows measured potentials of pristine and e-beam irradiated (exposed on the purple rectangular area) 1L-$MoTe_2$. Potential maps of 1L- and 3L-$MoTe_2$ for all process steps are shown in Figure S5, Supporting Information. We observed a clear reduction of surface potential by ≈100 mV with 20 kV beam irradiation as shown in black line profile of Figure 3b, comparing to pristine and annealed states. Considering the n-doping effect in electrical measurements (Figure 2), the reduced surface potential does not support a work-function modification of $MoTe_2$ since it indicates a p-type doping as seen from the annealed sample. Unlike our results, it is known that mild plasma treatment on 2D semiconductor can increase surface potential via vacancy formation such as Se vacancies in WSe_2, resulting in an n-doping effect.[37] Thus, vacancy formation cannot be a mechanism responsible for the doping.

Kumar et al. have investigated the effect of surface charge injection in rare-earth oxide thin film by KPFM measurements.[38] It was found that electron trap charges at the surface lowered the measured surface potential. Thus, we believe that the n-doping effect is attributed to trapped charges induced by e-beam irradiation. A recent paper has calculated the spatial distribution of electron energy with different acceleration voltages and found that the penetration depth of an e-beam is ≈10 nm with an acceleration voltage of 1 kV while it becomes much greater than 100 nm with an acceleration voltage > 10 kV.[20] We used 90 nm thick SiO_2 for this work. Thus, it is expected that electrons must penetrate through the entire oxide layer and escape through the doped Si which is grounded. Electrons possibly leave holes (electrons) behind at the interface between SiO_2 and Si ($MoTe_2$ and SiO_2) after the generation of electron–hole pairs as depicted in Figure 3c. To confirm this scenario, we measured surface potentials of e-beam irradiated $MoTe_2$ with different acceleration voltages, as shown in Figure 3b (surface potential maps are shown in Figure S6, Supporting Information). Significant reduction of surface potential was observed upon e-beam irradiation with an acceleration voltage of 20 kV while no clear difference in surface potential was observed with an acceleration voltage of 1 kV since penetration depth was much smaller than the oxide thickness and the energy was too low to generate sufficient electron–hole pairs. Accordingly, trapped charges induced by e-beam irradiation resulted in the reduction of potential and the n-doping effect in $MoTe_2$. Although the charges should not directly contribute to carrier transport as they are trapped at the

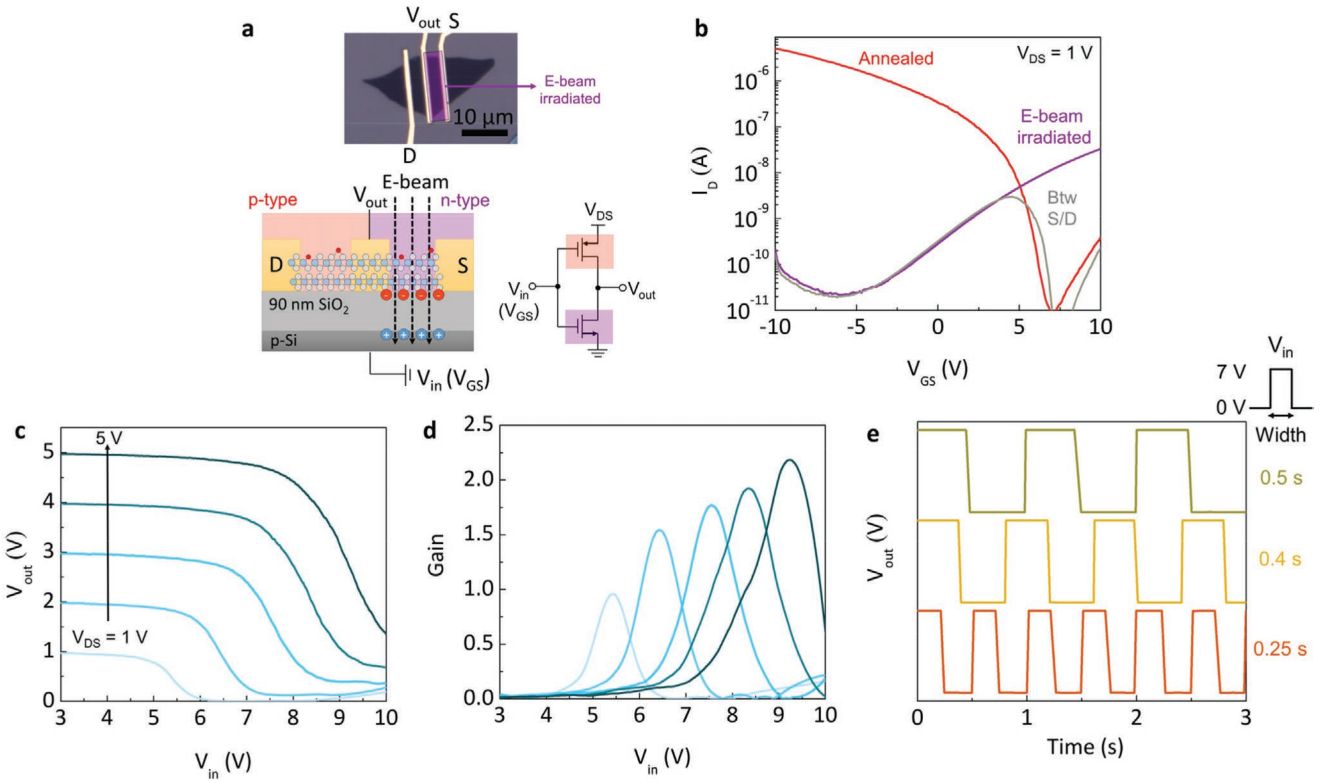

Figure 4. CMOS Inverter characteristics of $MoTe_2$. a) Optical micrograph and schematic and circuit diagrams of 3L-$MoTe_2$ CMOS inverter. b) Transfer curves of annealed (p-type), e-beam irradiated (n-type), and combined (p + n between S/D) devices. c) V_{out}–V_{in}, d) gain ($|dV_{out}/dV_{in}|$), and e) dynamic response characteristics of the inverter with 500 µC cm^{-2} e-beam irradiation.

interface, they can contribute to an electrostatic field across the oxide to n-dope the $MoTe_2$.

The doping mechanism of interface trap charges is further evidenced by large V_{GS} hysteresis measurements which can figure out the influences of charge trapping and de-trapping as shown in Figure 3d. A large perpendicular electric field applied across the SiO_2 at high V_{GS} can de-trap the trapped charges.[39] After V_{GS} sweeping in the increased range from –60 to +60 V, the transfer curve of $MoTe_2$ transistor showed a large positive V_{TH} shift as shown in blue curves. As shown in the inset, we observed a large leakage current only at high negative V_{GS}, indicating that the hole trapped charges at the interface between SiO_2/Si were de-trapped and then escaped through the ground along with the leakage path. We understand that this charge de-trapping process eliminates the n-doping effects contributing to the positive V_{TH} shift. Then, we can induce the n-doping by interface trap charges again upon subsequent e-beam irradiation as shown in purple curves. These repeatable charge trapping and de-trapping processes by e-beam irradiation and large V_{GS} sweeping support our proposed doping mechanism.

Since the trap charge-induced doping could reduce the surface potential irrespective of material and its thickness, 3L-$MoTe_2$ and graphene on 90 nm SiO_2/Si also showed a similar reduction of potential with 20 kV beam irradiation (Figure S7, Supporting Information). Furthermore, we fabricated and measured a WSe_2 device to determine whether e-beam irradiation could n-dope other 2D materials. Transition of polarity of the WSe_2 device from p-type to n-type was clearly observed after the irradiation as shown in Figure 3e, confirming the universal n-doping effect of e-beam irradiation. Thus, we can conclude that e-beam irradiation provides a general n-doping method for 2D devices by generating interface trap charges.

Selective n-doping by e-beam irradiation allowed us to fabricate a CMOS inverter as a basic building block of digital electronics composed of $MoTe_2$ p- and n-FETs. As shown in **Figure 4**a, a 3L-$MoTe_2$ device was first annealed to form p-FET. Subsequently, e-beam irradiation was selectively applied to form n-FET. Transfer characteristics of annealed, e-beam irradiated, and mixed $MoTe_2$ at V_{DS} = 1 V are shown in Figure 4b. A clear p-type semiconducting behavior was observed from the annealed sample (red). In contrast, an n-type behavior was observed for the e-beam irradiated $MoTe_2$ (purple), suggesting that e-beam could compensate hole carriers and induce excess electron carriers by trapped interface charges as expected from a larger estimated electron density induced by e-beam irradiation (2.68×10^{12} cm^{-2} after 10 loops of 500 µC cm^{-2} e-beam) than the hole density by annealing (4.7×10^{11} cm^{-2}). Despite carrier type conversion after e-beam irradiation, the lower ON-current of n-FET than that of p-FET attributed to the hole carrier compensation can be a drawback in CMOS circuits. This can be resolved if we use an intrinsic p-type semiconductor such as WSe_2 as evidenced from the symmetric n- and p-branch conductions in Figure 3e. However, we didn't include the WSe_2 CMOS inverter in this work as we mainly focused the doping effects in electrical characteristics of $MoTe_2$.

When the transfer characteristic was measured between source and drain (S/D) through both p- and n-FETs, a qualitative superposition of both FETs' characteristics (gray) was found. Output characteristics also showed a rectifying behavior when measured between S/D contacts, indicating the formation of p-n junction (Figure S8, Supporting Information). Figure 4c shows voltage transfer characteristic of the fabricated CMOS inverter. A small V_{in} saturated V_{out} to the applied V_{DS} while a large V_{in} made V_{out} become zero (ground voltage), which was an obvious inverter characteristic. Gain ($|dV_{out}/dV_{in}|$) as a figure of merit of the CMOS inverter had a peak >2 with the applied V_{DS} = 5 V as shown in Figure 4d. The gain was further enhanced to >10 by using graphite back-gate with relatively thin (≈40 nm) hexagonal boron nitride (*h*-BN) as shown in Figure S9, Supporting Information. Similar electron–hole pair generation induced by e-beam irradiation in *h*-BN and trap charges near interfaces presumably contributed to the n-doping. Figure 4e shows a dynamic response of the inverter with a pulse of 7 V and widths of 0.5, 0.4, and 0.25 s, showing a clear transition between "0" (ground) and "1" (V_{DS}) logic states of V_{out}. Our work demonstrated the successful fabrication of a $MoTe_2$ CMOS inverter with reliable and clean doping methods by wafer-scale processible annealing with subsequent selective e-beam irradiation. Consequently, this work can be extended for forming multiple arrays of inverters such as ring oscillators and logic processors using 2D semiconductors.

3. Conclusion

In this work, we presented chemical-free and clean doping methods for 2D $MoTe_2$ by annealing and e-beam irradiation. We found that the annealing p-doped $MoTe_2$ while the e-beam irradiation n-doped $MoTe_2$. Raman, KPFM, and electrical measurements revealed that the underlying doping mechanisms of annealing and e-beam irradiation were work-function modified by the absorption of oxygen molecules and charge trapping at interfaces, respectively. Interface trap charges induced by e-beam irradiation could be universal for a dopant as we observed similar n-doping effects in other 2D materials such as graphene and WSe_2. Finally, a $MoTe_2$ CMOS inverter that showed voltage transfer characteristics and dynamic response was fabricated using the proposed doping method of annealing with subsequent selective e-beam irradiation. This work provides a path to realize wafer-scale digital electronics using 2D semiconducting materials.

4. Experimental Section

Fabrication and Characterization of $MoTe_2$ Devices: $MoTe_2$ flakes (purchased from HQ Graphene) were placed on SiO_2/Si substrate by mechanical exfoliation. Thicknesses of these flakes were determined by optical contrast and AFM measurements. Metal patterns were formed using poly(methyl methacrylate) resist and e-beam lithography. Then 2 nm Cr/50 nm Au (the same metals were used for WSe_2 device in Figure 3e) was deposited using e-beam evaporation followed by metal lift-off using acetone. All electrical measurements were performed in vacuum (<10^{-3} Torr) using a semiconductor parameter analyzer (Agilent 4155C). To fabricate CMOS inverters, a RTA system was used with an annealing time of 3 h at 250 °C at a vacuum level of 5 mTorr to p-dope $MoTe_2$. Subsequently, selective e-beam irradiation was conducted for the same flakes to form an n-type region using an e-beam pattern generator attached to a FE-SEM system. Conditions for beam exposure were: areal step size of 0.05 µm, dwell time of 0.48 ms, beam current of 0.027 nA, acceleration voltage of 20 kV, and areal dose of 400–700 µC cm^{-2}. For $MoTe_2$ CMOS inverters, 10 loops of 500 µC cm^{-2} beam irradiation were used while other conditions remained the same. Raman spectroscopy was conducted using a micro-Raman spectroscopy system with a 532 nm laser to reveal the mechanism of doping. Dynamic responses of the inverter were measured using a parameter analyzer and a pulse generator. Peak voltage of 7 V, base voltage of 0 V, lead and tail of 0.1 µs, and width of 0.5, 0.4, and 0.25 s were used for the applied V_{in} pulses.

KPFM Measurements: KPFM consisting of an AFM was connected to an external lock-in amplifier to apply AC bias to an AFM tip. The tip was coated with highly conductive gold. A voltage of 2 V was applied to the tip through the lock-in amplifier at a frequency of 17.5 kHz. Metallic electrodes on the sample and chuck were connected to the ground of the equipment. The AFM body was placed in an electric field shielded box which was maintained at room temperature with a modest humidity <25%.

Acknowledgements

M.S.C. and M.L. contributed equally to this work. This work was supported by the Global Research Laboratory (GRL) Program (2016K1A1A2912707), the Basic Science Research Program (2021R1A2C2010869), and the Global Frontier Research Program (2013M3A6B1078873) funded by National Research Foundation of Korea (NRF).

Conflict of Interest

The authors declare no conflict of interest.

Data Availability Statement

Research data are not shared.

Keywords

2D materials, annealing, complementary metal-oxide-semiconductor, doping, electron beam irradiation

Received: May 20, 2021
Published online:

[1] G. Fiori, F. Bonaccorso, G. Iannaccone, T. Palacios, D. Neumaier, A. Seabaugh, S. K. Banerjee, L. Colombo, *Nat. Nanotechnol.* **2014**, *9*, 768.
[2] C. Choi, Y. Lee, K. W. Cho, J. H. Koo, D.-H. Kim, *Acc. Chem. Res.* **2019**, *52*, 73.
[3] G. Gawlik, P. Ciepielewski, J. Baranowski, *Appl. Sci.* **2019**, *9*, 544.
[4] V. P. Pham, G. Y. Yeom, *Adv. Mater.* **2016**, *28*, 9024.
[5] C. Ruppert, O. B. Aslan, T. F. Heinz, *Nano Lett.* **2014**, *14*, 6231.
[6] I. G. Lezama, A. Ubaldini, M. Longobardi, E. Giannini, C. Renner, A. B. Kuzmenko, A. F. Morpurgo, *2D Mater.* **2014**, *1*, 021002.
[7] D. Qu, X. Liu, M. Huang, C. Lee, F. Ahmed, H. Kim, R. S. Ruoff, J. Hone, W. J. Yoo, *Adv. Mater.* **2017**, *29*, 1606433.
[8] J. Liu, Y. Wang, X. Xiao, K. Zhang, N. Guo, Y. Jia, S. Zhou, Y. Wu, Q. Li, L. Xiao, *Nanoscale Res. Lett.* **2018**, *13*, 291.

[9] J. Y. Lim, A. Pezeshki, S. Oh, J. S. Kim, Y. T. Lee, S. Yu, D. K. Hwang, G.-H. Lee, H. J. Choi, S. Im, *Adv. Mater.* **2017**, *29*, 1701798.
[10] Y. J. Park, A. K. Katiyar, A. T. Hoang, J. Ahn, *Small* **2019**, *15*, 1901772.
[11] X. Liu, D. Qu, Y. Yuan, J. Sun, W. J. Yoo, *ACS Appl. Mater. Interfaces* **2020**, *12*, 26586.
[12] J. Chen, J. Zhu, Q. Wang, J. Wan, R. Liu, *Small* **2020**, *16*, 2001428.
[13] Y. Ke, X. Song, D. Qi, J. Liu, Q. Hao, Z. Wang, S. Tang, W. Zhang, *Adv. Electron. Mater.* **2020**, *6*, 2000532.
[14] T. Luo, B. Pan, K. Zhang, Y. Dong, C. Zou, Z. Gu, L. Zhang, *Appl. Surf. Sci.* **2021**, *540*, 148276.
[15] Y.-C. Lin, D. O. Dumcenco, Y.-S. Huang, K. Suenaga, *Nat. Nanotechnol.* **2014**, *9*, 391.
[16] Y. Katagiri, T. Nakamura, A. Ishii, C. Ohata, M. Hasegawa, S. Katsumoto, T. Cusati, A. Fortunelli, G. Iannaccone, G. Fiori, S. Roche, J. Haruyama, *Nano Lett.* **2016**, *16*, 3788.
[17] H.-P. Komsa, J. Kotakoski, S. Kurasch, O. Lehtinen, U. Kaiser, A. V. Krasheninnikov, *Phys. Rev. Lett.* **2012**, *109*, 035503.
[18] K. Elibol, T. Susi, G. Argentero, M. R. A. Monazam, T. J. Pennycook, J. C. Meyer, J. Kotakoski, *Chem. Mater.* **2018**, *30*, 1230.
[19] X. Yu, Y. Shen, T. Liu, T. Wu, J. Wang, *Q. Sci. Rep.* **2015**, *5*, 12014.
[20] W. Shi, S. Kahn, L. Jiang, S.-Y. Wang, H.-Z. Tsai, D. Wong, T. Taniguchi, K. Watanabe, F. Wang, M. F. Crommie, A. Zettl, *Nat. Electron.* **2020**, *3*, 99.
[21] P. M. Coelho, H.-P. Komsa, K. Lasek, V. Kalappattil, J. Karthikeyan, M.-H. Phan, A. V. Krasheninnikov, M. Batzill, *Adv. Electron. Mater.* **2019**, *5*, 1900044.
[22] H. Seo, D. Goo, G. Jung, How to Obtain Sample Potential Data for KPFM Measurement, https://parksystems.com (accessed: January **2021**).
[23] F. A. Rasmussen, K. S. Thygesen, *J. Phys. Chem. C* **2015**, *119*, 13169.
[24] C. Kim, I. Moon, D. Lee, M. S. Choi, F. Ahmed, S. Nam, Y. Cho, H.-J. Shin, S. Park, W. J. Yoo, *ACS Nano* **2017**, *11*, 1588.
[25] N. Ma, D. Jena, *2D Mater.* **2015**, *2*, 015003.
[26] D. S. Schulman, A. J. Arnold, S. Das, *Chem. Soc. Rev.* **2018**, *47*, 3037.
[27] S. B. Mitta, M. S. Choi, A. Nipane, F. Ali, C. Kim, J. T. Teherani, J. Hone, W. J. Yoo, *2D Mater.* **2020**, *8*, 012002.
[28] S. Cho, S. Kim, J. H. Kim, J. Zhao, J. Seok, D. H. Keum, J. Baik, D.-H. Choe, K. J. Chang, K. Suenaga, S. W. Kim, Y. H. Lee, H. Yang, *Science* **2015**, *349*, 625.
[29] C. Kim, S. Issarapanacheewin, I. Moon, K. Y. Lee, C. Ra, S. Lee, Z. Yang, W. J. Yoo, *Adv. Electron. Mater.* **2020**, *6*, 1900964.
[30] H. Zhu, Q. Wang, L. Cheng, R. Addou, J. Kim, M. J. Kim, R. M. Wallace, *ACS Nano* **2017**, *11*, 11005.
[31] Y.-M. Chang, S.-H. Yang, C.-Y. Lin, C.-H. Chen, C.-H. Lien, W.-B. Jian, K. Ueno, Y.-W. Suen, K. Tsukagoshi, Y.-F. Lin, *Adv. Mater.* **2018**, *30*, 1706995.
[32] Q. Liang, J. Gou, Arramel, Q. Zhang, W. Zhang, A. T. S. Wee, *Nano Res.* **2020**, *13*, 3439.
[33] Y. Zhou, J. Jadwiszczak, D. Keane, Y. Chen, D. Yu, H. Zhang, *Nanoscale* **2017**, *9*, 8657.
[34] M.-Y. Lu, S.-C. Wu, H.-C. Wang, M.-P. Lu, *Phys. Chem. Chem. Phys.* **2018**, *20*, 9038.
[35] T.-Y. Kim, K. Cho, W. Park, J. Park, Y. Song, S. Hong, W.-K. Hong, T. Lee, *ACS Nano* **2014**, *8*, 2774.
[36] E. Wu, Y. Xie, J. Zhang, H. Zhang, X. Hu, J. Liu, C. Zhou, D. Zhang, *Sci. Adv.* **2019**, *5*, eaav3430.
[37] M. Tosun, L. Chan, M. Amani, T. Roy, G. H. Ahn, P. Taheri, C. Carraro, J. W. Ager, R. Maboudian, A. Javey, *ACS Nano* **2016**, *10*, 6853.
[38] P. Kumar, R. Khosla, S. K. Sharma, *Surf. Interfaces* **2016**, *4*, 69.
[39] M. S. Choi, G.-H. Lee, Y.-J. Yu, D.-Y. Lee, S. H. Lee, P. Kim, J. Hone, W. J. Yoo, *Nat. Commun.* **2013**, *4*, 1624.